








## Research Article

# Largely Suppressed Magneto-Thermal Conductivity and Enhanced Magneto-Thermoelectric Properties in PtSn<sub>4</sub>

Chenguang Fu <sup>1</sup>, Satya N. Guin,<sup>1</sup> Thomas Scaffidi <sup>2,3</sup>, Yan Sun,<sup>1</sup> Rana Saha <sup>4</sup>, Sarah J. Watzman <sup>5</sup>, Abhay K. Srivastava <sup>4,6</sup>, Guowei Li,<sup>1</sup> Walter Schnelle,<sup>1</sup> Stuart S. P. Parkin,<sup>4</sup> Claudia Felser <sup>1</sup>, and Johannes Gooth <sup>1</sup>

<sup>1</sup>Max Planck Institute for Chemical Physics of Solids, 01187 Dresden, Germany

<sup>2</sup>Department of Physics, University of California, Berkeley, CA 94720, USA

<sup>3</sup>Department of Physics, University of Toronto, Toronto, Ontario M5S 1A7, Canada

<sup>4</sup>Max Planck Institute of Microstructure Physics, 06120 Halle, Germany

<sup>5</sup>Department of Mechanical and Materials Engineering, University of Cincinnati, Cincinnati, OH 45219, USA

<sup>6</sup>Institute of Physics, Martin Luther University Halle-Wittenberg, 06120 Halle, Germany

Correspondence should be addressed to Chenguang Fu; [chenguang.fu@cpfs.mpg.de](mailto:chenguang.fu@cpfs.mpg.de) and Johannes Gooth; [johannes.gooth@cpfs.mpg.de](mailto:johannes.gooth@cpfs.mpg.de)

Received 26 December 2019; Accepted 17 February 2020; Published 7 April 2020

Copyright © 2020 Chenguang Fu et al. Exclusive Licensee Science and Technology Review Publishing House. Distributed under a Creative Commons Attribution License (CC BY 4.0).

Highly conductive topological semimetals with exotic electronic structures offer fertile ground for the investigation of the electrical and thermal transport behavior of quasiparticles. Here, we find that the layer-structured Dirac semimetal PtSn<sub>4</sub> exhibits a largely suppressed thermal conductivity under a magnetic field. At low temperatures, a dramatic decrease in the thermal conductivity of PtSn<sub>4</sub> by more than two orders of magnitude is obtained at 9 T. Moreover, PtSn<sub>4</sub> shows both strong longitudinal and transverse thermoelectric responses under a magnetic field. Large power factor and Nernst power factor of approximately 80–100  $\mu\text{W}\cdot\text{cm}^{-1}\cdot\text{K}^{-2}$  are obtained around 15 K in various magnetic fields. As a result, the thermoelectric figure of merit  $zT$  is strongly enhanced by more than 30 times, compared to that without a magnetic field. This work provides a paradigm for the decoupling of the electron and hole transport behavior of highly conductive topological semimetals and is helpful for developing topological semimetals for thermoelectric energy conversion.

## 1. Introduction

In recent years, thermoelectric effects have attracted considerable attention in the fields of materials science and solid-state physics and chemistry. Practically, solid-state thermoelectric conversion offers a promising solution for energy harvesting and cooling [1]. Furthermore, investigations of thermoelectric phenomena are important for understanding the fundamental transport behavior of quasiparticles in solid materials [2]. The thermoelectric efficiency of a material is gauged by the figure of merit,  $zT = S^2T/\rho\kappa$ , where  $S$ ,  $T$ ,  $\rho$ , and  $\kappa$  are the thermopower, absolute temperature, electrical resistivity, and thermal conductivity, respectively. The term  $S^2/\rho$  is known as the thermoelectric power factor. Although the expression is simple, obtaining a high  $zT$  is a challenging task because these transport parameters are interrelated. As a

compromise, heavily doped semiconductors with moderate electrical conductivity and thermopower values have become the most widely investigated thermoelectric systems [3–5]. Metals or semimetals, owing to strong coupling of  $S$ ,  $\rho$ , and the electronic thermal conductivity  $\kappa_e$ , have attracted much less attention for thermoelectric studies. The key to developing metals or semimetals for thermoelectric application lies in the decoupling of the three electrical transport parameters.

In a two-carrier semimetal system, the thermopower  $S$  is expressed as  $(S_e\sigma_e + S_h\sigma_h)/(\sigma_e + \sigma_h)$ , where  $e$  and  $h$  indicate electrons and holes, respectively, and  $\sigma$  is the electrical conductivity.  $S_e$  and  $S_h$  generally have opposite signs and thus balance each other's contribution to  $S$ . Assuming the conduction and valence bands have symmetric structure and the Fermi level lies between them, the terms  $S_e\sigma_e$  and  $S_h\sigma_h$  will have similar values but opposite signs, so  $S$  will be almost

zero. Therefore, semimetals with symmetric conduction and valence bands have generally been viewed as poor thermoelectric materials. One way to overcome this disadvantage is to look for semimetals with a large asymmetry between the conduction and valence bands, where the large disparity in their electron and hole effective masses could ensure a sizable  $S$  [6, 7]. Another recently proposed method of generating a large thermopower in topological Dirac/Weyl semimetals is to apply a sufficiently large magnetic field, under which the thermopower will grow linearly without saturation [8]. These proposals suggest feasible ways to tune the thermoelectric properties of topological semimetals.

When a conductive solid is placed under a longitudinal temperature gradient and a transverse magnetic field, two types of thermoelectric responses occur, i.e., the magneto-Seebeck effect in the longitudinal direction and the Nernst effect in the other transverse direction [9]. Both longitudinal and transverse thermoelectric effects have recently received attention in the studies of topological semimetals, specifically, studies of giant magnetic-field enhancement of the thermoelectric properties [10, 11] or exploration of the Berry curvature-related anomalous thermoelectric transport phenomena [12–18]. For instance, in the Dirac semimetal  $\text{Cd}_3\text{As}_2$  [19], which has ultrahigh carrier mobility [20], anomalous magneto-Seebeck and Nernst effects were recently observed [12, 14], and the relationship between these anomalous transport properties with Berry curvature was discussed. Moreover, the magnetic-field-induced giant enhancement in both longitudinal and transverse  $zT$  values were found in  $\text{Cd}_3\text{As}_2$  single crystals near room temperature [11, 21, 22]. NbP, one of the first type-I Weyl semimetals to be discovered [23–25], has recently attracted attention as a material platform for exploring the Weyl physics-related thermoelectric transport properties. Large magneto-thermopower and Nernst thermopower were observed in both single crystals and polycrystalline samples [10, 16, 26]. These findings demonstrate that topological semimetals provide fertile ground for exploring magnetic-field-mediated thermoelectric properties. Moreover, recent high-throughput searches have identified thousands of topological semimetals in the Inorganic Crystal Structure Database [27–29]. Among them, those with complex crystal structure or heavy elements would display high potential for magneto-thermoelectric conversion, as they could have an intrinsically low phonon thermal conductivity.

In this work, we study the electrical and thermal transport properties of the Dirac semimetal  $\text{PtSn}_4$  under a magnetic field. The Dirac nodal arc structure and high magnetoresistance (MR) in  $\text{PtSn}_4$  suggest that the electrical properties will respond strongly to a magnetic field [30, 31]; furthermore, the layered structure with  $a-c$  planes stacked vertically along the  $b$  axis (Figure 1(a)) and low Debye temperature of 210 K [31] suggest a low phonon thermal conductivity, which however has not been reported. In our experiments, we used  $\text{PtSn}_4$  single crystals grown from a Sn-rich binary melt [31]. The growth process and chemical and structural characterizations are described in the Methods section. The electrical resistivity  $\rho$ , thermopower  $S$ , Nernst thermopower  $S_{xy}$ , Hall resistivity  $\rho_{\text{H}}$ , and thermal conductivity  $\kappa$  were measured at various magnetic fields,  $B$ , up to 9 T. The

details of the measurement procedure are also presented in the Methods section. All the transport experiments were conducted within the  $a-c$  plane of the crystals, and the magnetic field is applied along the  $b$  axis. The transport properties exhibited a dramatic response to the magnetic field below 30 K. When the magnetic field was applied, a large power factor of  $80\text{--}100\ \mu\text{W}\cdot\text{cm}^{-1}\cdot\text{K}^{-2}$  and a very large suppression of the thermal conductivity appeared, which together contribute to an obvious increase in the peak  $zT$  at 15 K. Moreover,  $\text{PtSn}_4$  also exhibits a strong Nernst signal and a large Nernst power factor of  $90\ \mu\text{W}\cdot\text{cm}^{-1}\cdot\text{K}^{-2}$  at 9 T and 10 K. These findings on  $\text{PtSn}_4$  provide a good paradigm for tuning highly conductive topological semimetals for simultaneous longitudinal and transverse thermoelectric energy conversion.

## 2. Results and Discussion

In the first set of transport experiments at zero magnetic field, we confirm that the  $\text{PtSn}_4$  crystals exhibit the previously observed low electrical resistivity  $\rho$ . In Figure 1(b), the measured  $\rho$  is shown as a function of  $T$ . In agreement with the literature [31],  $\rho(T)$  at zero field increases linearly with  $T$  between 25 and 300 K, as expected for such semimetals, in which electron-phonon scattering is thought to dominate. Below 8 K, the resistivity starts to saturate, with a residual resistivity of  $45\ \text{n}\Omega\cdot\text{cm}$  at 2 K. Furthermore, a high residual resistance ratio of  $\rho(300\ \text{K})/\rho(2\ \text{K}) \approx 1000$  is observed, which, together with the nonsaturating MR up to 9 T, indicates a long carrier mean free path.

The absolute thermopower of  $\text{PtSn}_4$  at 0 T is much lower than that of typical thermoelectric semiconductors.  $S(T)$  is positive at high  $T$  and exhibits a  $p-n$  transition upon cooling (Figure 1(c)), indicating that  $\text{PtSn}_4$  is a two-carrier semimetal system. When the magnetic field is applied,  $S$  depends strongly on  $B$  at approximately 14 K, in agreement with the literature [31]. As a result, a moderate thermopower  $S \approx -40\ \mu\text{V}\cdot\text{K}^{-1}$  at 9 T is obtained. Even though the magnetic field also induces strong MR, large peak power factors of  $80\text{--}100\ \mu\text{W}\cdot\text{cm}^{-1}\cdot\text{K}^{-2}$ , calculated by  $S^2/\rho$ , are obtained under various magnetic fields (Figure 1(d)). Recalling that good thermoelectric materials generally have relatively low power factor, for example,  $\text{Bi}_2\text{Te}_3$  ( $30\text{--}50\ \mu\text{W}\cdot\text{cm}^{-1}\cdot\text{K}^{-2}$ ) [32],  $\text{PbTe}$  ( $\approx 20\ \mu\text{W}\cdot\text{cm}^{-1}\cdot\text{K}^{-2}$ ) [33, 34],  $\text{SnSe}$  ( $\approx 10\ \mu\text{W}\cdot\text{cm}^{-1}\cdot\text{K}^{-2}$ ) [35],  $\text{CoSb}_3$  ( $30\text{--}50\ \mu\text{W}\cdot\text{cm}^{-1}\cdot\text{K}^{-2}$ ) [36], and half-Heusler compounds ( $30\text{--}50\ \mu\text{W}\cdot\text{cm}^{-1}\cdot\text{K}^{-2}$ ) [37], this large  $S^2/\rho$  observed in  $\text{PtSn}_4$  under a magnetic field indicates its potential for thermoelectric conversion.

A large enhancement in  $S^2/\rho$  is not the only required thermoelectric property; besides, the thermal conductivity should also be suppressed. We further measured the thermal conductivity  $\kappa$  of our samples as a function of temperature under various magnetic fields (Figure 1(e)). The experiments were performed with open electrical contact to prevent electric current flow.  $\kappa(T)$  indicates a metallic  $T$  dependence, which is consistent with the  $\rho$  and  $S$  measurements. Upon warming from 2 K,  $\kappa(T)$  increases linearly with  $T$  owing to the dominant impurity scattering. Near 8 K,  $\kappa(T)$  reaches a maximum and then starts to decrease. Remarkably,  $\kappa(T)$

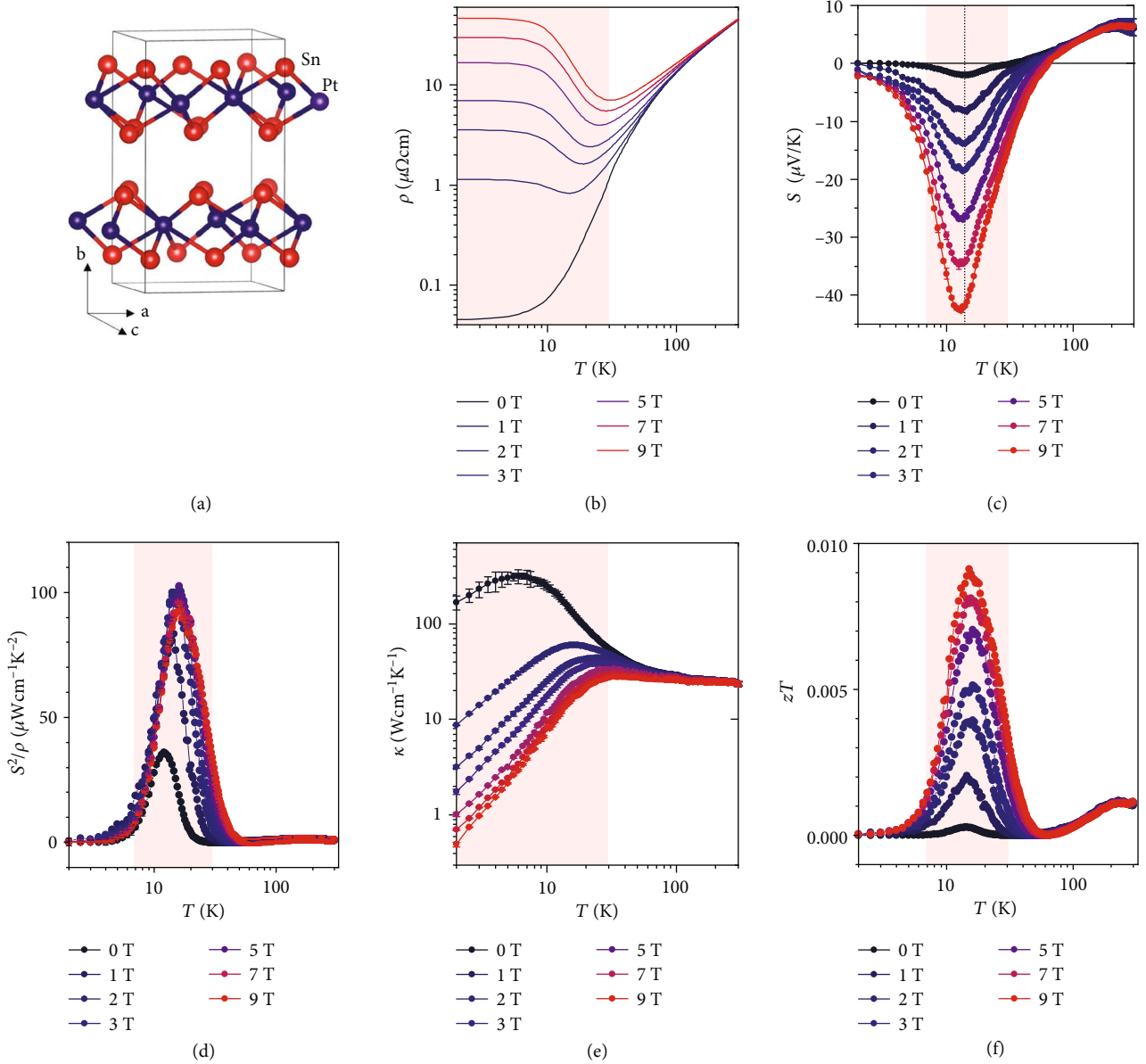


FIGURE 1: (a) Crystal structure of PtSn<sub>4</sub>. The chemical bonds indicate eight-fold Sn-coordinated Pt atoms. (b–f) Temperature dependence of electrical resistivity (b), thermopower (c), power factor (d), thermal conductivity (e), and  $zT$  (f) of PtSn<sub>4</sub> single crystals under various magnetic fields.

exhibits a rapid decay with increasing  $B$ . A decrease in  $\kappa(T)$  by more than 2 orders of magnitude is observed at 9 T and 2 K. This huge suppression of  $\kappa(T)$  is a result of the giant MR, which indicates that charge carriers, rather than phonons, dominate the thermal transport in PtSn<sub>4</sub>. Owing to the magnetic-field-induced giant reduction in  $\kappa$  and enhancement of  $S^2/\rho$ , PtSn<sub>4</sub> exhibits a peak  $zT$  of 0.009 at 9 T and 15 K (Figure 1(f)), which is more than 30 times higher than the  $zT$  at zero field. Note that this peak in  $zT$  is obtained at a very low temperature of 15 K. The  $z$  value, a more intrinsic material parameter reflecting the thermoelectric potential, is  $6 \times 10^{-4} \text{ K}^{-1}$  for PtSn<sub>4</sub> at 9 T and 15 K, which is close to that of good thermoelectric materials, for example, Bi<sub>2</sub>Te<sub>3</sub> ( $\approx 40 \times 10^{-4} \text{ K}^{-1}$ ) [32], PbTe ( $\approx 25 \times 10^{-4} \text{ K}^{-1}$ ) [33, 34],

CoSb<sub>3</sub> ( $\approx 20 \times 10^{-4} \text{ K}^{-1}$ ) [36], and half-Heusler compounds ( $\approx 10 \times 10^{-4} \text{ K}^{-1}$ ) [37]. More importantly, this very large increase in the peak  $zT$  of PtSn<sub>4</sub> results from the simultaneous improvement of  $S^2/\rho$  and suppression of  $\kappa$  with increasing  $B$ , which provides a good paradigm for the decoupling of the electrical and thermal transport properties.

To understand the magnetic-field-induced changes in the electrical transport properties, we further investigated the Hall resistivity  $\rho_H$  as a function of  $B$  at various  $T$ . Upon cooling from 300 K,  $\rho_H$  has a positive slope as a function of  $B$ , indicating that holes dominate the transport. Below 50 K, the slope of  $\rho_H(B)$  reverses its sign at high fields. Because  $d\rho_H(B)/dB$  changes sign at low temperatures, especially around 25 K, it is tempting to associate this phenomenon

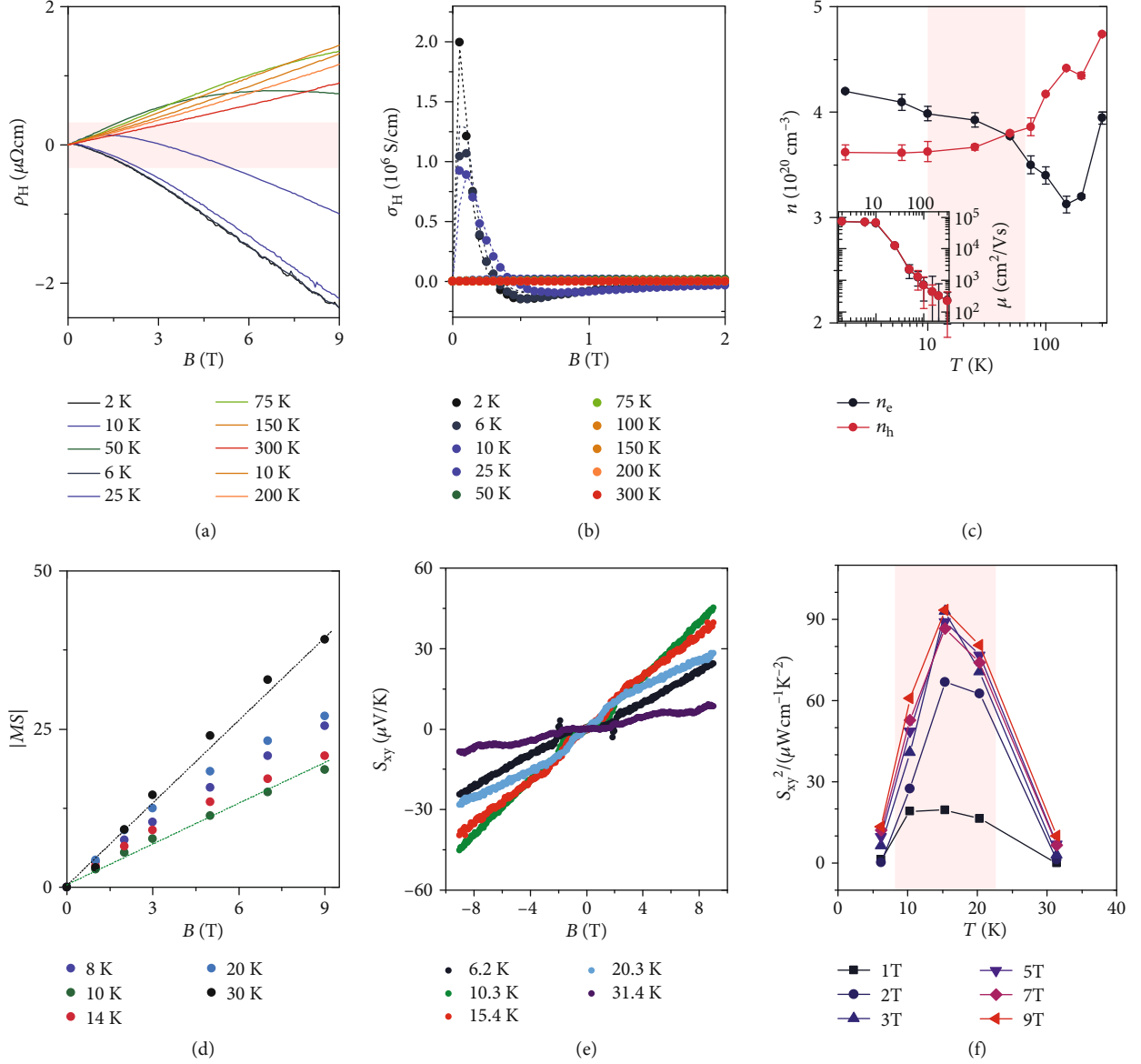


FIGURE 2: (a) Hall resistivity  $\rho_H(B)$  at various  $T$ . (b) Hall conductivity  $\sigma_H = \rho_H / (\rho_H^2 + \rho^2)$  at various  $T$ . The symbols represent the experimental data, and the dotted lines are fits according to a two-carrier model. (c) Carrier densities  $n_e$ ,  $n_h$  and mobilities  $\mu_e$ ,  $\mu_h$  as a function of  $T$  for electrons and holes, respectively. The lines are guides to the eyes. The error bars represent the fitting error. (d) Absolute magneto-thermopower  $|MS| = |[S(B) - S(0T)]/S(0T)|$  at various  $T$ . The dotted lines indicate linear fits. (e) Nernst thermopower  $S_{xy}$  as a function of  $B$  at various temperatures. (f) Nernst power factor  $S_{xy}^2/\rho$  as a function of  $T$  at various  $B$ .

with the transport contributions of both electrons and holes, which is also reflected by its thermopower at similar temperatures with almost  $0 \mu\text{V}\cdot\text{K}^{-1}$ . Moreover, the Fermi surface of  $\text{PtSn}_4$  was calculated using density functional theory (Figure S1) and also indicates that  $\text{PtSn}_4$  is a two-carrier system with multiple electron and hole pockets.

For a more quantitative analysis of the carrier densities and mobilities, we calculated the Hall conductivity,  $\sigma_H = \rho_H / (\rho_H^2 + \rho^2)$  (Figure 2(b)) using a two-carrier model:

$$\sigma_H(B) = \left[ \frac{n_h^2 \mu_h^2}{1 + \mu_h^2 B^2} - \frac{n_e^2 \mu_e^2}{1 + \mu_e^2 B^2} \right] eB. \quad (1)$$

This model enables us to obtain the temperature-dependent average carrier densities,  $n_e$ ,  $n_h$  and the carrier mobilities  $\mu_e$ ,  $\mu_h$  for the electron and hole pockets, respectively. The best fits to our data indeed reveal that our  $\text{PtSn}_4$  samples exhibit parallel transport of both electrons and holes across the full temperature range investigated (Figure 2(c)), with a hole excess above 50 K and an electron excess below. The electron and hole mobilities are very high (Figure 2(c), inset) and are comparable to those of the other topological semimetals [20, 25], in which the high mobility are responsible for the giant MR observed at low  $T$  (Figure 1(b)).

After determining the carrier densities, we further investigated the thermopower as a function of  $B$  around the

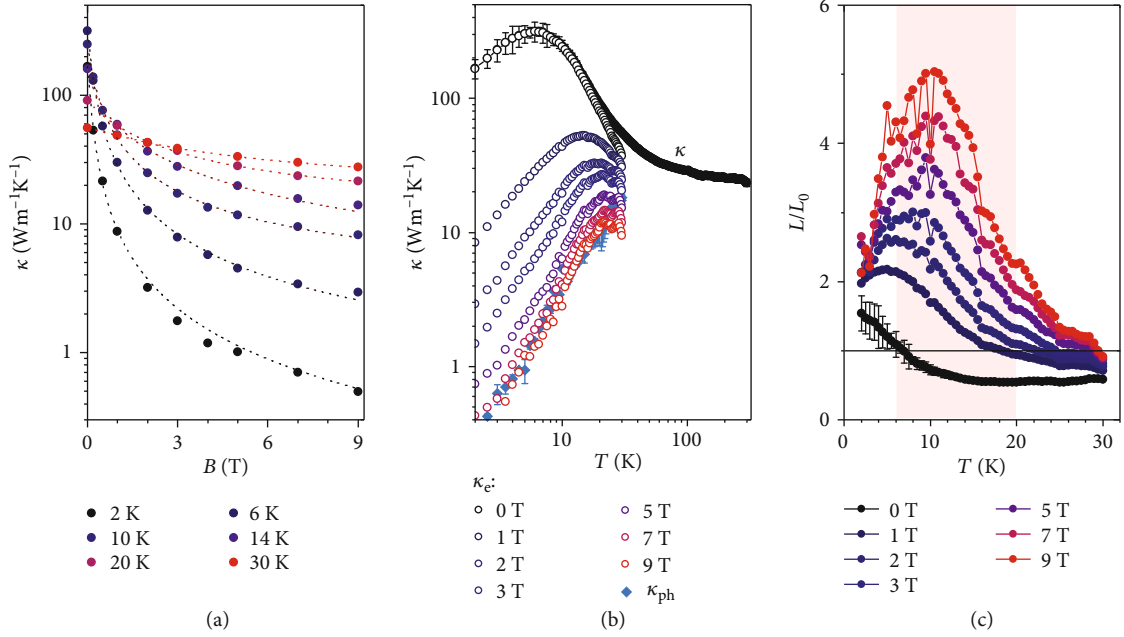


FIGURE 3: (a) Thermal conductivity  $\kappa$  as a function of  $B$  at various  $T$ . The dotted lines represent fits of  $\kappa(B, T) = \kappa_{ph}(T) + \kappa_e(T)/(1 + \eta B^s)$  to the data. (b) Extracted  $\kappa_{ph}$  and  $\kappa_e(B)$  under various magnetic fields. (c) Lorenz number  $L$ , scaled by the Sommerfeld value  $L_0$ , as a function of  $T$  at various  $B$ .

temperatures at which  $S$  peaks. As shown in Figure 2(d), a dramatic enhancement of  $S$  occurs with increasing  $B$ . The absolute magneto-thermopower,  $|\text{MS}| = |[S(B) - S(0\text{ T})]/S(0\text{ T})|$ , becomes significant at higher magnetic fields ( $B > 3\text{ T}$ ), exhibiting an approximately linear relationship with  $B$ . The linear relationship at high magnetic fields can be understood in terms of the increase in the electron-phonon scattering rate with  $B$  [38], yielding  $|\text{MS}| \approx \hbar\omega_c/k_B T$  for  $\hbar\omega_c > k_B T$ , where  $\hbar$  and  $k_B$  are the reduced Planck and Boltzmann constants, respectively. In addition,  $\omega_c = eB/m_{e/h}^*$  denotes the cyclotron frequency, where  $e$  is the elementary charge. For an average effective mass,  $m_{e/h}^* = 0.2m_e$ , a linear relation between  $|\text{MS}|$  and  $B$  is expected above 3 T, in agreement with the experiments.

Considering the large carrier mobilities below 30 K and the strong response of the longitudinal thermopower to a magnetic field, it is tempting to check for the transverse thermoelectric response, i.e., the Nernst effect. The Nernst thermopower  $S_{xy}$  of PtSn<sub>4</sub> at various temperatures was further measured by a standard one-heater, two-thermometer configuration. As shown in Figure 2(e),  $S_{xy}$  displays a normal Nernst signal, namely, an approximately linear increase upon magnetic-field application, and no saturation is found at magnetic fields of up to 9 T. At 9 T and 10.3 K,  $S_{xy}$  reaches a moderate value of  $45\ \mu\text{V}\cdot\text{K}^{-1}$ . Furthermore, because the electrical resistivity in the  $a-c$  plane is approximately isotropic [39], the Nernst power factor can be estimated as  $S_{xy}^2/\rho$  (Figure 2(f)). Like the conventional power factor (Figure 1(d)), the Nernst power factor also peaks at approximately 15 K. A maximum value of approximately  $90\ \mu\text{W}\cdot\text{cm}^{-1}\cdot\text{K}^{-2}$  is obtained at various magnetic fields,

which is approximately 3 times larger than the value obtained in polycrystalline bulk NbP [10].

The thermal conductivity  $\kappa$  as a function of  $B$  is shown in Figure 3(a). At 2 K, as the magnetic field increases,  $\kappa(B)$  decreases by more than 2 orders of magnitude. The phonon thermal conductivity of a metallic system typically does not change significantly under a magnetic field. The very large decrease in  $\kappa(B)$  is thus a result of the large MR (Figure 1(b)), which then makes it possible to separate the phonon and electron components of the thermal conductivity. An empirical expression,  $\kappa(B, T) = \kappa_{ph}(T) + \kappa_e(T)/(1 + \eta B^s)$  [40, 41], was employed to extract the phonon thermal conductivity,  $\kappa_{ph}(T)$ , and electron thermal conductivity,  $\kappa_e(T)$ , at 0 T, where  $\eta$  and  $s$  are related to the thermal mobility and scattering mechanism, respectively. The obtained fitting parameters are shown in Table S1. Because this method is generally effective for large  $\mu B$ , only the  $\kappa(B, T)$  data below 30 K were fitted. The fitted lines match the experimental data well, as shown in Figure 3(a), indicating the feasibility of this method. The extracted  $\kappa_e(B, T)$  decreases continuously with increasing  $B$ , as shown in Figure 3(b). At  $B = 0\text{ T}$ ,  $\kappa_e(T)$  is significantly larger than  $\kappa_{ph}(T)$ , demonstrating that PtSn<sub>4</sub> is indeed a metallic system in which charge carriers dominate the electrical and thermal transport properties. The Lorenz number  $L$  is further calculated according to the Wiedemann–Franz (WF) law [1], as shown in Figure 3(c). At  $B = 0\text{ T}$ , this is a downward violation of the WF law, whereas an upward violation is found when the magnetic field is applied. Violations of the WF law typically indicate inelastic electron-phonon scattering or hydrodynamic

transport, as recently found in the Weyl semimetal  $WP_2$  [42, 43]. Moreover, in a very recent work on another Weyl semimetal system, TaP, Han et al. also observed an upward violation of the WF law [40]. The reason is still not clear, but it seems that violation of the WF law under a magnetic field is common in topological semimetals.

### 3. Conclusions

In summary, measurements of the electrical and thermal transport properties established  $PtSn_4$  as a distinctive platform by exhibiting strong regulation of the two-carrier transport behavior under both a thermal gradient and a magnetic field.  $PtSn_4$  is a highly conductive topological semimetal with low electrical resistivity at liquid helium temperatures, which is comparable to that of many well-established metals or topological semimetals [44]. Hall effect measurement of  $PtSn_4$  revealed a two-carrier behavior with both high electron and high hole mobilities. At zero magnetic field, the thermopower is close to zero, and the thermal conductivity is orders of magnitude higher than that of good thermoelectric semiconductors. These features indicate that  $PtSn_4$  has a poor thermoelectric performance.

However, all these transport properties change significantly when a magnetic field is applied. Large Seebeck and Nernst power factors and a huge suppression of the thermal conductivity are simultaneously realized under various magnetic fields, providing a good example for decoupling the electrical and thermal transport properties of semimetals. These dramatic changes in the transport properties are the result of the regulation of the transport behavior of the two types of carriers under a magnetic field. At zero magnetic field, the thermal gradient drives the accumulation of both electrons and holes on the cold side, which balance each other's contributions to the Seebeck thermopower. When a magnetic field is applied, the electrons and holes exhibit different transport behaviors, which makes it possible to realize strong thermoelectric responses in both the longitudinal and transverse directions. These results on  $PtSn_4$  provide a paradigm for tuning highly conductive semimetals for both longitudinal and transverse thermoelectric conversion by applying a magnetic field. Interestingly, some recent work had paid attention to the relationship between thermoelectric performance and internal magnetic interactions, for example, superparamagnetic behavior [45], paramagnon drag [46], and spin fluctuation [47]. These works together with our current study on  $PtSn_4$  demonstrate that introducing magnetic interaction as an additional influence on the transport properties, either by applying an external magnetic field or by introducing an internal magnetic moment, could open a new direction in thermoelectric research.

### 4. Experimental Methods

Single crystals of  $PtSn_4$  were grown from a Sn-rich binary melt as described in the literature [31]. The high-purity starting elements, Pt (shot, 99.99%) and Sn (shot, 99.999%), were mixed with an initial stoichiometry of  $Pt_4Sn_{96}$ ; the mixture was placed in an alumina crucible, which was sealed in a

quartz tube under partial Ar pressure. The quartz tube was heated to 600°C over a period of 5 h and held at that temperature for 20 h. Next, it was slowly cooled to 350°C over a period of 60 h. The excess Sn flux was removed using a centrifuge at 400°C. After centrifugation, the remaining flux on the surface was removed by mechanical polishing.

Powder X-ray diffraction measurement of  $PtSn_4$  was performed using  $Cu K\alpha$  radiation at room temperature to identify the phase purity and crystal structure. An image-plate Huber G670 Guinier camera was used in a diffraction range of  $10^\circ \leq 2\theta \leq 100^\circ$  in steps of  $0.005^\circ$ . Scanning electron microscopy (SEM) with energy-dispersive X-ray spectrometry (EDXS) was used for elemental analysis. Single-crystal X-ray diffraction measurements were performed using a Bruker D8 Venture diffractometer with  $Mo K\alpha$  radiation and the SHELX97 software was used for structure refinement [48]. More information about the crystallographic and refinement parameters can be found in our previous work [49], where the studied  $PtSn_4$  single crystal is from the same batch with the current work. The crystal structure is described by the centrosymmetric space group  $Ccca$ , in agreement with the literature [50]. Figure 1(a) shows the layered crystal structure of  $PtSn_4$ , which consists of  $PtSn_4$  slabs constructed from eight-fold Sn-coordinated Pt atoms. The layered structure is visible in the SEM results, as shown in Figure S2. The layered nature of  $PtSn_4$  allows for slight disorder in the ac plane, i.e., a small misalignment between consecutive  $PtSn_4$  layers.

The powder X-ray diffraction pattern of  $PtSn_4$  is shown in Figure S3. The diffraction peaks can be well indexed to orthorhombic structure, in good agreement with the single-crystal X-ray diffraction results [49]. No other obvious phases are observed. The actual composition of the  $PtSn_4$  single crystal is determined by EDXS at seven randomly selected positions; the result agrees with the nominal composition within the instrument error, as shown in Table S2. High-resolution transmission electron microscopy (HRTEM) (Figure S4) of a  $6.7 \mu m \times 4.4 \mu m$  lamella showed the good crystallinity of the  $PtSn_4$  sample (Figure S5).

The temperature-dependent thermal conductivity and thermopower under a magnetic field were jointly measured adiabatically by the one-heater, two-thermometer configuration using the thermal transport option of the PPMS (Quantum Design), in which the sample was placed so that the magnetic field was perpendicular to the heat flow. The thermometers were calibrated under the magnetic field using the PPMS MR calibration wizard before the thermal transport measurements. To ensure uniform heat flow through the bar-shaped sample, two gold-plated copper leads were attached to both ends of the sample using silver epoxy and then connected to the heater and sink, respectively. Two other copper leads were wrapped around and glued to the sample with silver epoxy for detecting  $\Delta V$  and  $\Delta T$ . The applied temperature gradients were approximately 1%–3% of the base temperature. We then investigated the possible effect of the thermal contact resistances and demonstrated the need for careful contact preparation. After careful contact preparation, as described above, we investigated samples

with lengths ranging from 4.5 to 7 mm, but similar cross-sections and contact areas. We obtained consistent results for all the samples at any magnetic field or temperature investigated, and therefore did not observe any indication of diminished thermal conductivity owing to contact. The Nernst thermopower was also measured adiabatically in the one-heater, two-thermometer configuration using the PPMS. The Nernst signal was estimated as,  $S_{xy} = L_x V_y / L_y \Delta T_x$ , where  $L_x$  is the distance between the two temperature leads,  $L_y$  is the distance between the two voltage wires,  $V_y$  is the transverse electric voltage, and  $\Delta T_x$  is the measured temperature difference. The measured raw Nernst thermopower data were antisymmetrized to correct for contact misalignment.

Both the longitudinal and Hall resistivities were measured by a standard four-probe method using the AC transport option in the PPMS system with an applied AC current of 16 mA. Point contacts for Hall voltage probes were obtained by spot-welding 25  $\mu\text{m}$  platinum wires. For the current and longitudinal voltage probes, linear contacts were made using silver paint and platinum wires. To correct for contact misalignment, the measured Hall resistivity was field antisymmetrized. For all the transport measurements, the magnetic field was applied along the  $b$  axis, which was perpendicular to the  $a - c$  plane.

## Conflicts of Interest

The authors declare no competing financial interest.

## Acknowledgments

We acknowledge Jonah Weissman, Sean Hartnoll, and Subir Sachdev for valuable discussions, Machteld E. Kamminga for performing the single-crystal XRD studies, and Peter Werner for the help with TEM. This work was financially supported by the ERC advanced grant No. (742068) “TOP-MAT”. Ch.F. and S.N.G. acknowledge financial support from the Alexander von Humboldt Foundation. T.S. acknowledges support from the Emergent Phenomena in Quantum Systems initiative of the Gordon and Betty Moore Foundation. A.K.S. was funded by the Deutsche Forschungsgemeinschaft (DFG, German Research Foundation)—project number 314790414. M.E.K. was supported by The Netherlands Organization for Science NWO (graduate program 2013, No. 022.005.006).

## Supplementary Materials

Fermi surface, SEM images, TEM images, XRD pattern, and EDX results. (*Supplementary Materials*)

## References

- [1] H. J. Goldsmid, *Introduction of Thermoelectricity*, Springer, Heidelberg, 2010.
- [2] K. Behnia, *Fundamentals of Thermoelectricity*, Oxford University Press, Oxford, 2015.
- [3] T. Zhu, Y. Liu, C. Fu, J. P. Heremans, J. G. Snyder, and X. Zhao, “Compromise and synergy in high-efficiency thermoelectric materials,” *Advanced Materials*, vol. 29, no. 14, article 1605884, 2017.
- [4] T. Mori, “Novel principles and nanostructuring methods for enhanced thermoelectrics,” *Small*, vol. 13, no. 45, article 1702013, 2017.
- [5] J. Mao, Z. Liu, J. Zhou et al., “Advances in thermoelectrics,” *Advances in Physics*, vol. 67, no. 2, pp. 69–147, 2018.
- [6] M. Markov, X. Hu, H. C. Liu et al., “Semi-metals as potential thermoelectric materials,” *Scientific Reports*, vol. 8, no. 1, p. 9876, 2018.
- [7] J. Mao, H. Zhu, Z. Ding et al., “High thermoelectric cooling performance of n-type  $\text{Mg}_3\text{Bi}_2$ -based materials,” *Science*, vol. 365, no. 6452, pp. 495–498, 2019.
- [8] B. Skinner and L. Fu, “Large, nonsaturating thermopower in a quantizing magnetic field,” *Science Advances*, vol. 4, no. 5, article eaat2621, 2018.
- [9] K. Behnia and H. Aubin, “Nernst effect in metals and superconductors: a review of concepts and experiments,” *Reports on Progress in Physics*, vol. 79, no. 4, article 046502, 2016.
- [10] C. Fu, S. N. Guin, S. J. Watzman et al., “Large Nernst power factor over a broad temperature range in polycrystalline Weyl semimetal NbP,” *Energy & Environmental Science*, vol. 11, no. 10, pp. 2813–2820, 2018.
- [11] H. Wang, X. Luo, W. Chen et al., “Magnetic-field enhanced high-thermoelectric performance in topological Dirac semimetal  $\text{Cd}_3\text{As}_2$  crystal,” *Science Bulletin*, vol. 63, no. 7, pp. 411–418, 2018.
- [12] Z. Jia, C. Li, X. Li et al., “Thermoelectric signature of the chiral anomaly in  $\text{Cd}_3\text{As}_2$ ,” *Nature Communications*, vol. 7, no. 1, article 13013, 2016.
- [13] X. Li, L. Xu, L. Ding et al., “Anomalous Nernst and Righi-Leduc effects in  $\text{Mn}_3\text{Sn}$ : Berry curvature and entropy flow,” *Physical Review Letters*, vol. 119, no. 5, article 056601, 2017.
- [14] T. Liang, J. Lin, Q. Gibson et al., “Anomalous Nernst Effect in the Dirac Semimetal  $\text{Cd}_3\text{As}_2$ ,” *Physical Review Letters*, vol. 118, no. 13, article 136601, 2017.
- [15] A. Sakai, Y. P. Mizuta, A. A. Nugroho et al., “Giant anomalous Nernst effect and quantum-critical scaling in a ferromagnetic semimetal,” *Nature Physics*, vol. 14, no. 11, pp. 1119–1124, 2018.
- [16] S. J. Watzman, T. M. McCormick, C. Shekhar et al., “Dirac dispersion generates unusually large Nernst effect in Weyl semimetals,” *Physical Review B*, vol. 97, no. 16, article 161404, 2018.
- [17] S. N. Guin, K. Manna, J. Noky et al., “Anomalous Nernst effect beyond the magnetization scaling relation in the ferromagnetic Heusler compound  $\text{Co}_2\text{MnGa}$ ,” *NPG Asia Materials*, vol. 11, no. 1, article 16, 2019.
- [18] S. N. Guin, P. Vir, Y. Zhang et al., “Zero-field Nernst effect in a ferromagnetic Kagome-Lattice Weyl-semimetal  $\text{Co}_3\text{Sn}_2\text{S}_2$ ,” *Advanced Materials*, vol. 31, no. 25, article 1806622, 2019.
- [19] Z. Wang, H. Weng, Q. Wu, X. Dai, and Z. Fang, “Three-dimensional Dirac semimetal and quantum transport in  $\text{Cd}_3\text{As}_2$ ,” *Physical Review B*, vol. 88, no. 12, article 125427, 2013.
- [20] T. Liang, Q. Gibson, M. N. Ali, M. Liu, R. J. Cava, and N. P. Ong, “Ultra-high mobility and giant magnetoresistance in the Dirac semimetal  $\text{Cd}_3\text{As}_2$ ,” *Nature Materials*, vol. 14, no. 3, pp. 280–284, 2014.
- [21] H. Wang, X. Luo, K. Peng et al., “Magnetic field-enhanced thermoelectric performance in Dirac semimetal  $\text{Cd}_3\text{As}_2$

- crystals with different carrier concentrations,” *Advanced Functional Materials*, vol. 29, no. 37, article 1902437, 2019.
- [22] J. Xiang, S. L. Hu, M. Lyu et al., “Large transverse thermoelectric figure of merit in a topological Dirac semimetal,” *Science China Physics, Mechanics & Astronomy*, vol. 63, no. 3, article 237011, 2020.
- [23] H. Weng, C. Fang, Z. Fang, B. A. Bernevig, and X. Dai, “Weyl semimetal phase in noncentrosymmetric transition-metal monophosphides,” *Physical Review X*, vol. 5, no. 1, article 011029, 2015.
- [24] S.-Y. Xu, I. Belopolski, N. Alidoust et al., “Discovery of a Weyl fermion semimetal and topological Fermi arcs,” *Science*, vol. 349, no. 6248, pp. 613–617, 2015.
- [25] C. Shekhar, A. K. Nayak, Y. Sun et al., “Extremely large magnetoresistance and ultrahigh mobility in the topological Weyl semimetal candidate NbP,” *Nature Physics*, vol. 11, no. 8, pp. 645–649, 2015.
- [26] U. Stockert, R. D. Dos Reis, M. O. Ajeesh et al., “Thermopower and thermal conductivity in the Weyl semimetal NbP,” *Journal of Physics: Condensed Matter*, vol. 29, no. 32, article 325701, 2017.
- [27] M. G. Vergniory, L. Elcoro, C. Felser, N. Regnault, B. A. Bernevig, and Z. Wang, “A complete catalogue of high-quality topological materials,” *Nature*, vol. 566, no. 7745, pp. 480–485, 2019.
- [28] F. Tang, H. C. Po, A. Vishwanath, and X. Wan, “Comprehensive search for topological materials using symmetry indicators,” *Nature*, vol. 566, no. 7745, pp. 486–489, 2019.
- [29] T. Zhang, Y. Jiang, Z. Song et al., “Catalogue of topological electronic materials,” *Nature*, vol. 566, no. 7745, pp. 475–479, 2019.
- [30] Y. Wu, L. L. Wang, E. Mun et al., “Dirac node arcs in PtSn<sub>4</sub>,” *Nature Physics*, vol. 12, no. 7, pp. 667–671, 2016.
- [31] E. Mun, H. Ko, G. J. Miller, G. D. Samolyuk, S. L. Bud’ko, and P. C. Canfield, “Magnetic field effects on transport properties of PtSn<sub>4</sub>,” *Physical Review B*, vol. 85, no. 3, article 035135, 2012.
- [32] B. Poudel, Q. Hao, Y. Ma et al., “High-thermoelectric performance of nanostructured bismuth antimony telluride bulk alloys,” *Science*, vol. 320, no. 5876, pp. 634–638, 2008.
- [33] Y. Pei, X. Shi, A. LaLonde, H. Wang, L. Chen, and G. J. Snyder, “Convergence of electronic bands for high performance bulk thermoelectrics,” *Nature*, vol. 473, no. 7345, pp. 66–69, 2011.
- [34] K. Biswas, J. He, I. D. Blum et al., “High-performance bulk thermoelectrics with all-scale hierarchical architectures,” *Nature*, vol. 489, no. 7416, pp. 414–418, 2012.
- [35] P.-P. Shang, J. Dong, J. Pei et al., “Highly textured N-type SnSe polycrystals with enhanced thermoelectric performance,” *Research*, vol. 2019, article 9253132, 10 pages, 2019.
- [36] X. Shi, J. Yang, J. R. Salvador et al., “Multiple-filled Skutterudites: high thermoelectric figure of merit through separately optimizing electrical and thermal transports,” *Journal of the American Chemical Society*, vol. 133, no. 20, pp. 7837–7846, 2011.
- [37] C. Fu, T. Zhu, Y. Liu, H. Xie, and X. Zhao, “Band engineering of high performance p-type FeNbSb based half-Heusler thermoelectric materials for figure of merit  $zT > 1$ ,” *Energy & Environmental Science*, vol. 8, no. 1, pp. 216–220, 2015.
- [38] T. Ohta, “Phonon-drag Seebeck effect in a strong magnetic field (1) longitudinal case,” *Journal of the Physical Society of Japan*, vol. 18, no. 8, pp. 1166–1173, 1963.
- [39] M. Inamdar, M. Kriegisch, L. Shafeek et al., “Quantum oscillations in ultra pure PtSn<sub>4</sub>,” *Solid State Phenomena*, vol. 194, pp. 88–91, 2012.
- [40] F. Han, N. Andrejevic, T. Nguyen et al., “Discovery of giant, non-saturating thermopower in topological semimetal at quantum limit,” 2019, <http://arxiv.org/abs/1904.03179>.
- [41] R. Ocaña and P. Esquinazi, “Thermal conductivity tensor in YBa<sub>2</sub>Cu<sub>3</sub>O<sub>7-x</sub>: effects of a planar magnetic field,” *Physical Review B*, vol. 66, no. 6, 2002.
- [42] J. Gooth, F. Menges, N. Kumar et al., “Thermal and electrical signatures of a hydrodynamic electron fluid in tungsten diphosphide,” *Nature Communications*, vol. 9, no. 1, article 4093, 2018.
- [43] A. Jaoui, B. Fauqué, C. W. Rischau et al., “Departure from the Wiedemann–Franz law in WP<sub>2</sub> driven by mismatch in  $T$ -square resistivity prefactors,” *npj Quantum Materials*, vol. 3, no. 1, article 64, 2018.
- [44] J. Hu, S. Y. Xu, N. Ni, and Z. Mao, “Transport of topological semimetals,” *Annual Review of Materials Research*, vol. 49, no. 1, pp. 207–252, 2019.
- [45] W. Zhao, Z. Liu, Z. Sun et al., “Superparamagnetic enhancement of thermoelectric performance,” *Nature*, vol. 549, no. 7671, pp. 247–251, 2017.
- [46] Y. Zheng, T. Lu, M. M. H. Polash et al., “Paramagnon drag in high thermoelectric figure of merit Li-doped MnTe,” *Science Advances*, vol. 5, no. 9, article eaat9461, 2019.
- [47] N. Tsujii, A. Nishide, J. Hayakawa, and T. Mori, “Observation of enhanced thermopower due to spin fluctuation in weak itinerant ferromagnet,” *Science Advances*, vol. 5, no. 2, article eaat5935, 2019.
- [48] G. M. Sheldrick, *Program for Crystal Structure Refinement*, University of Göttingen, Göttingen, 1997.
- [49] G. Li, C. Fu, W. Shi et al., “Dirac nodal arc semimetal PtSn<sub>4</sub>: an ideal platform for understanding surface properties and catalysis for hydrogen evolution,” *Angewandte Chemie*, vol. 131, no. 37, pp. 13241–13246, 2019.
- [50] B. Künnen, D. Niepmann, and W. Jeitschko, “Structure refinements and some properties of the transition metal stannides Os<sub>3</sub>Sn<sub>7</sub>, Ir<sub>5</sub>Sn<sub>7</sub>, Ni<sub>0.402(4)</sub>Pd<sub>0.598</sub>Sn<sub>4</sub>,  $\alpha$ -PdSn<sub>2</sub> and PtSn<sub>4</sub>,” *Journal of Alloys and Compounds*, vol. 309, no. 1–2, pp. 1–9, 2000.